nature materials

Article

https://doi.org/10.1038/s41563-023-01722-x

Fast cycling of lithium metal in solid-state batteries by constriction-susceptible anode materials

Received: 12 December 2022

Accepted: 9 October 2023

Published online: 08 January 2024

Check for updates

Luhan Ye[1,2], Yang Lu[1,2], Yichao Wang[1], Jianyuan Li[1] & Xin Li[1]

Interface reaction between lithium (Li) and materials at the anode is not well understood in an all-solid environment. This paper unveils a new phenomenon of constriction susceptibility for materials at such an interface, the utilization of which helps facilitate the design of an active three-dimensional scaffold to host rapid plating and stripping of a significant amount of a thick Li metal layer. Here we focus on the well-known anode material silicon (Si) to demonstrate that, rather than strong Li–Si alloying at the conventional solid–liquid interface, the lithiation reaction of micrometre-sized Si can be significantly constricted at the solid–solid interface so that it occurs only at thin surface sites of Si particles due to a reaction-induced, diffusion-limiting process. The dynamic interaction between surface lithiation and Li plating of a family of anode materials, as predicted by our constrained ensemble computational approach and represented by Si, silver (Ag) and alloys of magnesium (Mg), can thus more homogeneously distribute current densities for the rapid cycling of Li metal at high areal capacity, which is important in regard to solid-state battery application.

The lithium (Li) metal anode, due to its tenfold larger capacity than commercial graphite anode, is a desired component for solid-state batteries. Fast cycling of commercial levels of thick cathode, however, is challenging because it requires rapid plating and stripping of a thick layer of Li metal at the anode, stably and without Li dendrite penetration. Although silicon (Si) anode voltage is higher than that of Li metal, its high capacity remains attractive. However, the Si anode often suffers from 300% volume change following lithiation, with swelling and pulverization[1–3], which limits its practical implementation in liquid-electrolyte batteries, although the issue can be alleviated by nano-engineering of the electrode including nanoparticles, nanowires or other nanostructures[4–6].

Here we show that the behaviour of micrometre-sized Si can be markedly different in solid-state batteries, where the alloying reaction can be constricted at shallow surface sites (~65 nm) of Si particles by a reaction strain-induced, diffusion-limiting process. A Si composite protection layer can thus host significant amount of Li metal plating that can accommodate ultrafast cycling of commercial-level cathode loading with high areal capacity, as demonstrated by our design of coin and pouch cells that utilizes the susceptibility of Si to the constriction.

Our ab initio, high-throughput simulations suggest that, among 59,524 material entries, Si and other promising materials, such as silver (Ag) and alloys of magnesium (Mg), are located in a unique region in the space of lithiation voltage versus constriction susceptibility, where susceptibility refers to the ability of a material to dynamically suppress the lithiation reaction in exchange for the Li plating one in solid-state battery design. These materials show a well-balanced constriction susceptibility and voltage and locate at the boundary of maximum product of the two factors in the parameter space. Such kinetically preferred Li plating occurs through the interaction dynamics between lithiation and plating, leading to a more homogeneous distribution of local current density at the anode. Our work thus provides a critical understanding that paves the way for the design of advanced Li metal

[1]John A. Paulson School of Engineering and Applied Sciences, Harvard University, Cambridge, MA, USA. [2]These authors contributed equally: Luhan Ye, Yang Lu. e-mail: lixin@seas.harvard.edu

https://doi.org/10.1038/s41563-023-01722-x

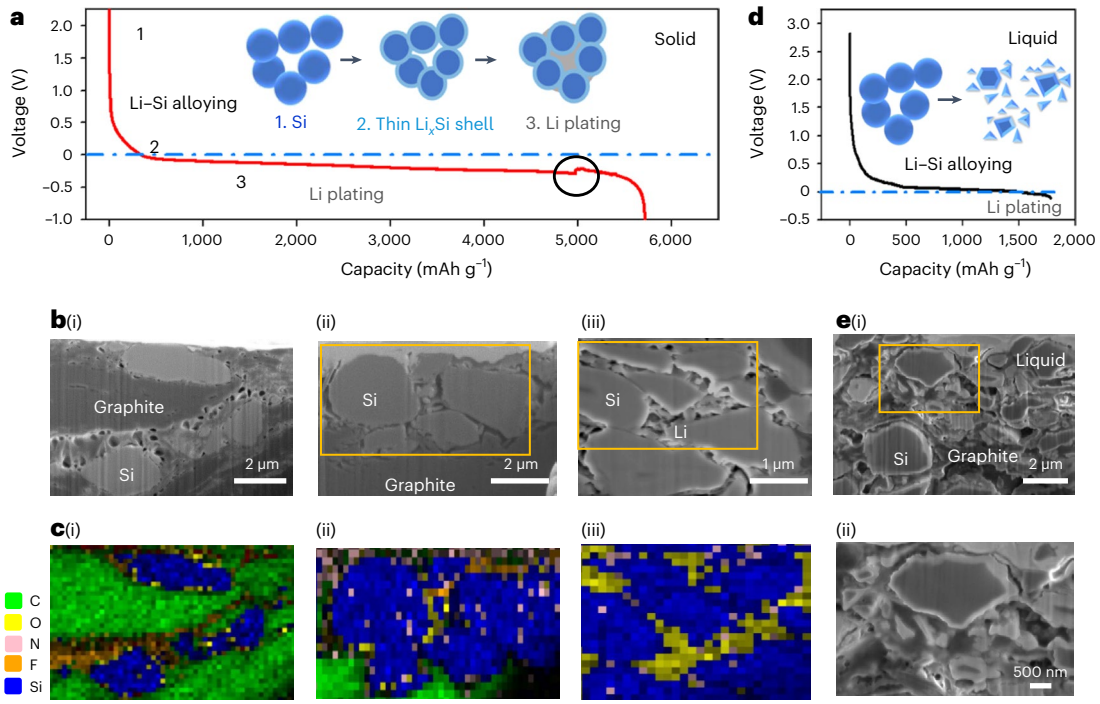

Fig. 1 | Significant Li plating capacity from Si anode. a, Li discharge profile in a battery of Li/graphite–$Li_{5.5}PS_{4.5}Cl_{1.5}$ (LPSCl1.5)–LGPS–LPSCl1.5–SiG at current density 0.2 mA cm^{-2} at room temperature. Note that SiG was made by mixing Si and graphite in one composite layer. Inset shows the schematic illustration of stages 1–3 based on SEM and EDS mapping, which illustrate the unique Li–Si anode evolution in solid-state batteries observed experimentally in Figs. 1 and 2. **b**, FIB–SEM images of the SiG anode at different discharge states (i), (ii) and (iii) corresponding to points 1–3 in **a**, respectively. **c**, SEM–EDS mapping of (i), (ii) and (iii), corresponding to SEM images in **b**, where carbon signal (C) is derived from graphite, oxygen (O) and nitrogen (N) signals are from Li metal reaction with air and fluorine (F) is from the PTFE binder. **d**, Discharge profile of battery with cell construction Li-1M $LiPF_6$ in EC/DMC–SiG. Schematics illustrate typical Si anode evolution in liquid-electrolyte batteries. **e**, FIB–SEM image (i) of SiG anode following discharge in the liquid-electrolyte battery shown in **d**; zoomed-in image (ii).

solid-state batteries for rapid cycling at high cathode loadings, by utilizing the constriction susceptibility of anode materials.

Li plating between Si particles with limited alloying

Figure 1a shows the specific capacity at room temperature of a solid-state asymmetric battery with a configuration of Li/graphite (G)–solid electrolytes (SEs)–SiG, where SiG is the composite layer formed by micrometre-sized Si and graphite particles. The discharge capacity—that is, moving Li^+ from Li/G to SiG—is >5,600 milliampere-hours per gram mass (mAh g^{-1}) if calculated based on the mass loading of Si, which is abnormally higher than its theoretical capacity of 4,200 mAh g^{-1} (around 3,000 mAh g^{-1} experimentally at most). At three different discharged states, focused-ion beam-scanning electron microscopy (FIB–SEM) images were recorded and energy-dispersive spectrum (EDS) mapping carried out (Fig. 1b) to reveal anode morphology and chemistry. Before discharge, the pristine anode showed pores between Si particles (Fig. 1b(i)); following discharge near 0 V, Si particles showed neither cracks nor any obvious swelling (Fig. 1b(ii),(iii)).

Marked Li deposition had already been observed between Si particles at −0.2 V (Fig. 1b(iii)), where the existence of Li metal was identified by its morphology and oxygen signal (Fig. 1c(iii)), because Li metal is the most reactive component in the composite with oxygen and nitrogen in the atmosphere[7]. Further evidence can be found in Extended Data Fig. 1. In addition, considering that maximum capacity is <0 V at such a very slow discharge of 0.2 mA cm^{-2} with little polarization, the above results suggest that there is significant Li plating at SiG and thus the composite may not serve as a typical Si anode. Towards the end of Li plating, at around 5,000 mAh g^{-1}, a short circuit was observed (circled region in Fig. 1a), which is a common phenomenon when there is a high level of Li deposition in a Li metal anode.

In contrast to the abnormal behaviour of the above solid-state batteries, in the liquid-electrolyte battery micrometre-sized Si particles exhibited normal plateaux at 0.5 and 0.3 V (versus Li/Li^+), corresponding to two Li-alloying reactions (Fig. 1d) with an expected total lithiation capacity around 1,800 mAh g^{-1}. SEM further showed a completely different morphology from Si pulverization that is common in liquid-electrolyte batteries for a Si anode (Fig. 1e). Further evidence showing such a difference in the SiG anode in solid and liquid-electrolyte batteries following cycling when paired with a $LiNi_{0.83}Mn_{0.06}Co_{0.11}O_2$ (NMC83) cathode can be found in Extended Data Fig. 2. The fact that no pulverization was observed in solid-state batteries (Fig. 1b and Extended Data Fig. 2d–f) suggests that lithiation of Si is largely limited and that significant capacity is provided by Li metal plating and stripping.

We then tried to detect Li distribution more directly in the anode. Although Li as a light element cannot be detected by EDS, electron energy-loss spectroscopy (EELS) and X-ray photoelectron spectroscopy (XPS) can capture it. We thus first combined an EELS line scan with EDS mapping in a scanning transmission electron microscope (STEM) to show Li distribution in the SiG composite anode (Fig. 2a–c). Figure 2a shows the dark-field STEM image of a SiG anode from a full battery paired with a thick NMC83 cathode after 500 cycles and stopped at a charged state of 4.1 V (Extended Data Fig. 2f). The SiG anode was milled to 65 nm thickness by FIB. Scanning from the vacuum region to the bulk of the Si particle (Fig. 2a), the Li–K edge in EELS (Fig. 2b) demonstrates that only the region at the surface of the Si particle shows the existence of Li. The absence of a Li EELS signal inside the Si particle indicates that a major portion of Si was not lithiated in battery cycling. Li–Si alloying should be limited to a skin surface layer of <65 nm thickness, as indicated by the region with coexisting Si–L and Li–K EELS signals in Fig. 2b.

https://doi.org/10.1038/s41563-023-01722-x

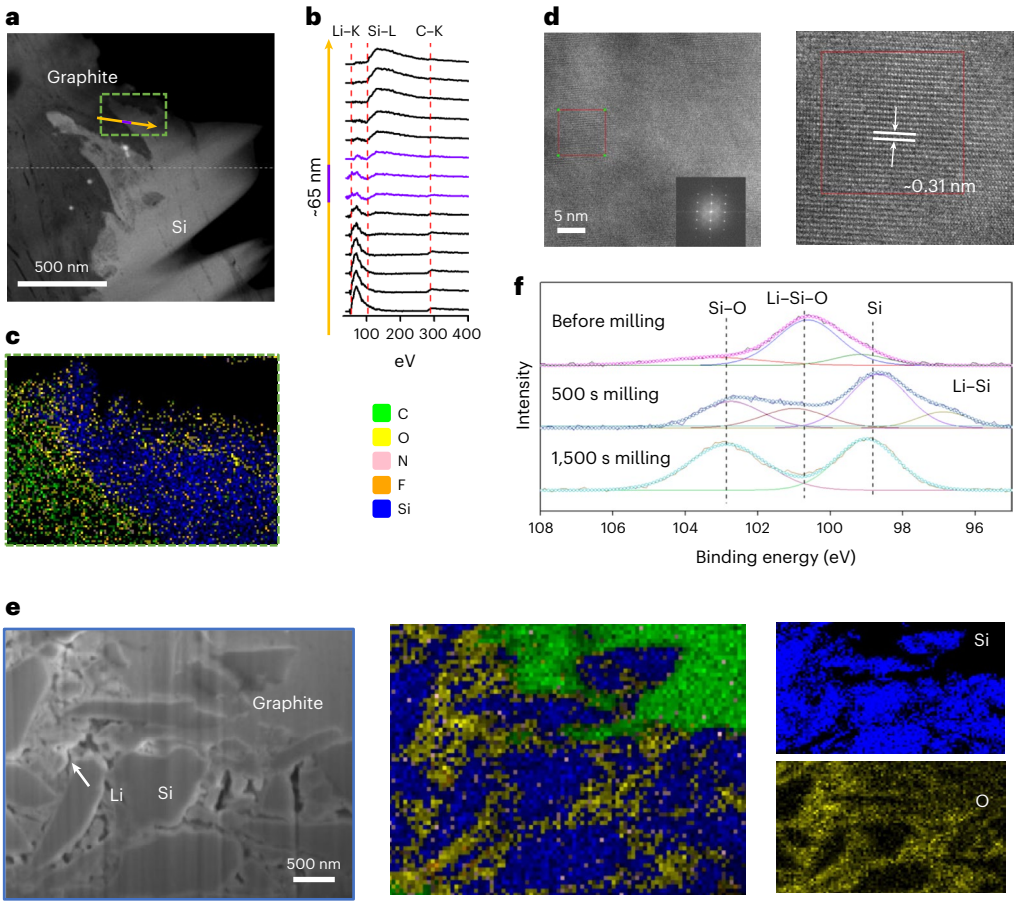

Fig. 2 | Thin lithiation shell of Si particles and forced plating of Li metal. **a**, TEM image of SiG anode FIB sample from a battery cycled at 2 C-rate (30 min charge or discharge) and 55 °C and stopped at the 500th charged state. The structure of the battery is Li-SiG–SEs–NMC83, with a nominal NP ratio of 1.5. **b**, EELS line scan across the yellow arrow line in **a**. The purple spectra correspond to the purple section in the arrow line at the surface of Si particle. **c**, STEM–EDS mapping of the green dashed-border area in **a**. **d**, Left, high-resolution TEM of a Si particle following FIB; right, zoomed-in image. **e**, FIB–SEM images (left) and EDS mapping (middle) of SiG anode at the first discharge state (2.5 V, 0.5 C-rate at room temperature) in solid-state battery with structure SiG–SEs–NMC83 and nominal NP ratio of 1.5. No Li was below the SiG anode. **f**, XPS depth profile of the SiG anode following full discharge of the battery in Fig. 1a; Li/G–SEs–SiG was discharged at current density 0.2 mA cm^{-2} at room temperature.

STEM–EDS mapping was conducted on the same sample (Fig. 2c), where the oxygen and nitrogen signals showed consistent distribution to the Li element from EELS, all outside Si particles. The high-resolution TEM image (Fig. 2d) shows the lattice fringe of the (111) plane with a measured *d* spacing of 3.1 Å, agreeing well with the pristine Si crystalline phase[8]. Furthermore, micrometre-sized Si particles maintained an intact morphology with no cracks, either after cycling at the charged state (Fig. 2c; STEM) or at discharge (Fig. 2e and Extended Data Fig. 3; SEM). They also showed a well-separated, rather than overlapped, distribution of EDS signals from oxygen (representing Li), carbon (from graphite) and Si from these full batteries (Fig. 2c,e and Extended Data Fig. 3c,f), consistent with the result from asymmetric batteries of Li/G–SEs–SiG (Fig. 1c). SEM and EDS taken at larger scale across the anode are displayed in Extended Data Fig. 4 for both pure Si (Extended Data Fig. 4a–l) and SiG (Extended Data Fig. 4m–q) anodes. The depth distribution of Li deposition shows that Li is preferentially plated in voids between Si particles or at the current collector side of the Si or SiG layer, rather than at the electrolyte–anode interface at 0.5 C-rate charge of full batteries.

Figure 2f shows XPS depth profile measurement around Si peak energy following stripping of all Li from the Li anode and plating to the SiG side in a SiG–SEs–G/Li solid-state battery, with a large discharge capacity of >5,000 mAh g^{-1}. Although the Li–Si–O peak was detected on the Si surface initially, following milling by Ar ions for 500 s (~26 nm) the signal of Li–Si–O reduced and Si, Li–Si and Si–O signals emerged. Following 1,500 s of milling (~78 nm), both Li–Si–O and Li–Si signals disappeared with only Si and Si–O peaks remaining. This XPS depth profile indicates that the lithiation reaction front locates at shallow depth, between 26 and 78 nm beneath the surface of Si particles, while the inner part is still pristine Si phase, consistent with our STEM–EELS and X-ray diffraction (XRD) results. More such evidence from XPS and XRD analysis can be found in Extended Data Fig. 5.

Therefore we confirm that, in our solid-state batteries, the lithiation of Si particles is largely limited. Meanwhile, Si particles serve as a scaffold to host Li metal plating and stripping with significant capacity in the void region between particles. However, different from an inert three-dimensional (3D) structure with merely pores inside, Li–Si alloying was still active in a skin surface layer of each Si particle, making our SiG layer an 'active' 3D scaffold.

Constriction susceptibility of anode material for Li plating

Silicone represents a family of materials at the anode in an all-solid-state environment, where the original lithiation capacity can be largely suppressed by the mechanical constriction effect when particle size is near micrometre size or above. In an all-solid environment, just like all other interface reactions with positive reaction strain (that is, $\varepsilon > 0$)[9–12], lithiation of the anode material has to overcome the local mechanical

constriction effect enforced by the effective constriction modulus, or simply effective modulus, of the material (K_{eff}).

In particular, K_{eff} contains a contribution from the kinetic diffusion-limiting effect induced by lithiation reaction (Methods). The positive reaction strain from local reaction sites (for example, local decomposition or lithiation) will compress the unreacted region of a particle, largely limiting ionic diffusion at the reaction front under compressive strain and thus preventing further reaction (Fig. 3a). Note that such a local point contact for Li-ion diffusion and reaction, which is common at the solid–solid interface (for example, between Si particles and between Li metal and Si or SE), will provide inhomogeneous Li chemical potential at nanoscale, which is critical in generating reaction front and strain field with large local curvature so that the unreacted particle material can wrap the reacted region to constrict and lock the local strain field.

From our nudged elastic band simulations (Fig. 3b), an isotropic compressive strain in Si from 5 to 10% readily increased the Li diffusion barrier from 0.4 to 0.8 eV, giving a 10^7-fold reduction in Li diffusivity in all diffusion directions at the reaction front. Alternatively, when we maintained a 5% compressive strain but added a small shear strain to one direction (Fig. 3b; $\beta = 80°$), diffusivity was also effectively reduced in all directions.

In contrast, in liquid electrolyte the Li ions are extremely homogeneous surrounding particles at the liquid–solid interface, giving orders of magnitude more homogeneous local Li chemical potential. This will lead to deeper reaction from homogeneous propagation of the much flatter reaction front, with much freer expansion of reaction strain into the liquid region.

The marked difference between a liquid-electrolyte and solid-state environment in the Li–Si interaction was also further evidenced from a specially designed experiment. We pressed Li metal foil and Si particle layers together to let them react and then measured XRD evolution over time. From the full-width at half-maximum (FWHM) change versus Bragg angle, clear strain broadening (Fig. 3a) was observed following 10 min of reaction[13,14] (Fig. 3c). After 20–40 h, although size broadening became more prominent, probably due to the formation of microcracks at the thin surface region induced by further increase in Li composition, the level of broadening was still very limited (ΔFHWM = ~0.10–0.15°; Fig. 3c,d). In contrast, for the liquid, size broadening already predominated in the first 10 min, giving a two- to threefold higher ΔFHWM of 0.25°. After 20 h size broadening had increased to 0.45° and, after 30 h, Si XRD peaks become too broad to measure (Fig. 3d). This further suggests that, although the surface lithiation composition of Si particles in the solid-state case could have increased over time to cause a limited level of broadening, lithiation into the particle core was still largely limited by strain field at the reaction front. Thus, the reaction front did not propagate more deeply and no further cracks formed in the Si particle core, yielding a low average lithiation capacity of the entire Si particle (that is, 200 mAh g^{-1} >0 V in Fig. 1a) and a low overall level of cracks. Original XRD data and further details can be found in Extended Data Fig. 6a–e.

The simulated theoretical lithiation capacity of Si (Fig. 3e) rapidly reduced from 4,000 mAh g^{-1} at K_{eff} = 0 GPa (that is, the theoretical capacity of Si) to ~1,000–2,000 mAh g^{-1} at mechanical constriction of K_{eff} = ~1–3 GPa and effective stress of ϵK_{eff} = ~1.2–1.5 GPa, which is the capacity range of Si particle in a liquid environment or Li–Si alloying thin shell of Si particle in a solid environment. The effective stress contains mainly local stress σ_{loc} in the liquid case, while it also contains increasing contribution from the kinetic diffusion-limiting process towards the reaction front in the solid case, providing constriction to the Li–Si alloying reaction. Capacity was further reduced to 164 mAh g^{-1} at K_{eff} = 5 GPa and to 0 mAh g^{-1} at K_{eff} = 5.5 GPa. This defines a critical modulus to fully suppress lithiation reaction of K_{crit} = 5.5 GPa, which is applied to the Si side of the frozen reaction front through local expansion of the Li–Si alloying region. Thus, the effective contribution from the kinetic stability effect, $\epsilon K_e^{D\to 0} = \epsilon K_{eff} - \sigma_{loc}$, is estimated to be comparable to the local stress at reaction front (see Methods for more details). Note that ϵK_{eff} at reaction front here is thus neither the external pressure in operating battery devices at MPa level nor the actual local stress around 1–2 GPa from lithiation, but rather reflects the property of Li interaction dynamics in an all-solid environment.

With the lithiation capacity of Si being rapidly suppressed by mechanical constriction, which includes both thermodynamic metastability from lithiation strain energy and kinetic stability from the lithiation reaction-induced, diffusion-limiting process in a solid-state battery (Methods), Li metal plating is forced to occur through the dynamic interaction between lithiation and plating at those shallow lithiation nanosites at the Si particle surface (Fig. 3a), which helps more homogeneously distribute plating current densities at the anode. Note that Li metal has a yield modulus of only a few megapascals[15,16] and thus plated Li can invade voids and pores between Si particles[15].

When we applied such an analysis to all material entries in the Materials Project, the plot in Fig. 3f provides new insights. For every material there is a corresponding critical modulus, K_{crit}, beyond which the lithiation reaction is prohibited[10]. Materials with low K_{crit} are thus more likely to suppress lithiation for plating by mechanical constriction. Note that low K_{crit} is also related to high reaction strain, which is one contributory factor to an effective diffusion limit at the reaction front (Fig. 3a). For two materials with the same K_{crit}, the one with higher lithiation composition at zero constriction thus means that more lithiation is suppressed per unit K_{crit}. Here the lithiation composition per K_{crit} that we introduce as the horizontal axis in Fig. 3f is thus a new metric describing the constriction susceptibility of a material. When this metric is plotted together with lithiation voltage as the vertical axis, an informative parameter space is created to distribute all 59,524 materials that we computed in the anode voltage range (Fig. 3f). These materials are all in a region with the boundary well described by a reciprocal function (Methods). In contrast, such a clear-cut boundary is not well defined in a conventional plot of voltage versus lithiation composition (Extended Data Fig. 6f). Because lithiation energy per atom is the product of lithiation composition and voltage, materials at such a boundary region described by reciprocal curves thus exhibit close lithiation energy per Li per unit constriction and the highest possible such values among all materials, which are around 0.35–0.55 eV GPa^{-1} per Li, setting the upper limit of dynamic energy exchange between lithiation and plating by mechanical constriction. We note that Si is located at the boundary region and shows a well-balanced voltage and constriction susceptibility.

Near the boundary region between the dashed lines in Fig. 3f there are 11,568 material entries. Elemental statistical analysis shows a high frequency of Mg, Si, Ge, Sn, In, Al and Ag in these materials (Fig. 3f, inset), and also the coappearance of, for example, Mg + Si, Mg + O or Mg + Sn (Extended Data Fig. 6g). A discussion about Mg_2Si can be found in Extended Data Fig. 6h, showing the negative effect of overly high constriction susceptibility and overly low lithiation voltage (Fig. 3f). Meanwhile, the abundance of Mg-related entries here, as highlighted for some Mg alloys in the region around Si, also suggests abundant opportunities regarding the design of Mg-based compounds for enhanced balance between the two metrics for such anode applications. Another, extreme, case is exemplified by Cu and Ti, which lack lithiation capacity (Fig. 3f). Due to the absence of reaction these do not have such a mechanism to distribute current densities and thus will more readily assist Li dendrite growth at certain randomly concentrated sites (Extended Data Fig. 6i).

Rapid cycling performance at high areal capacity

We now focus on the most readily availabe material, Si, to enable state-of-the-art cycling performance of the Li metal anode by utilizing the constriction susceptibility effect at high cathode loading or areal capacity in both coin and pouch solid-state cells. When using a

https://doi.org/10.1038/s41563-023-01722-x

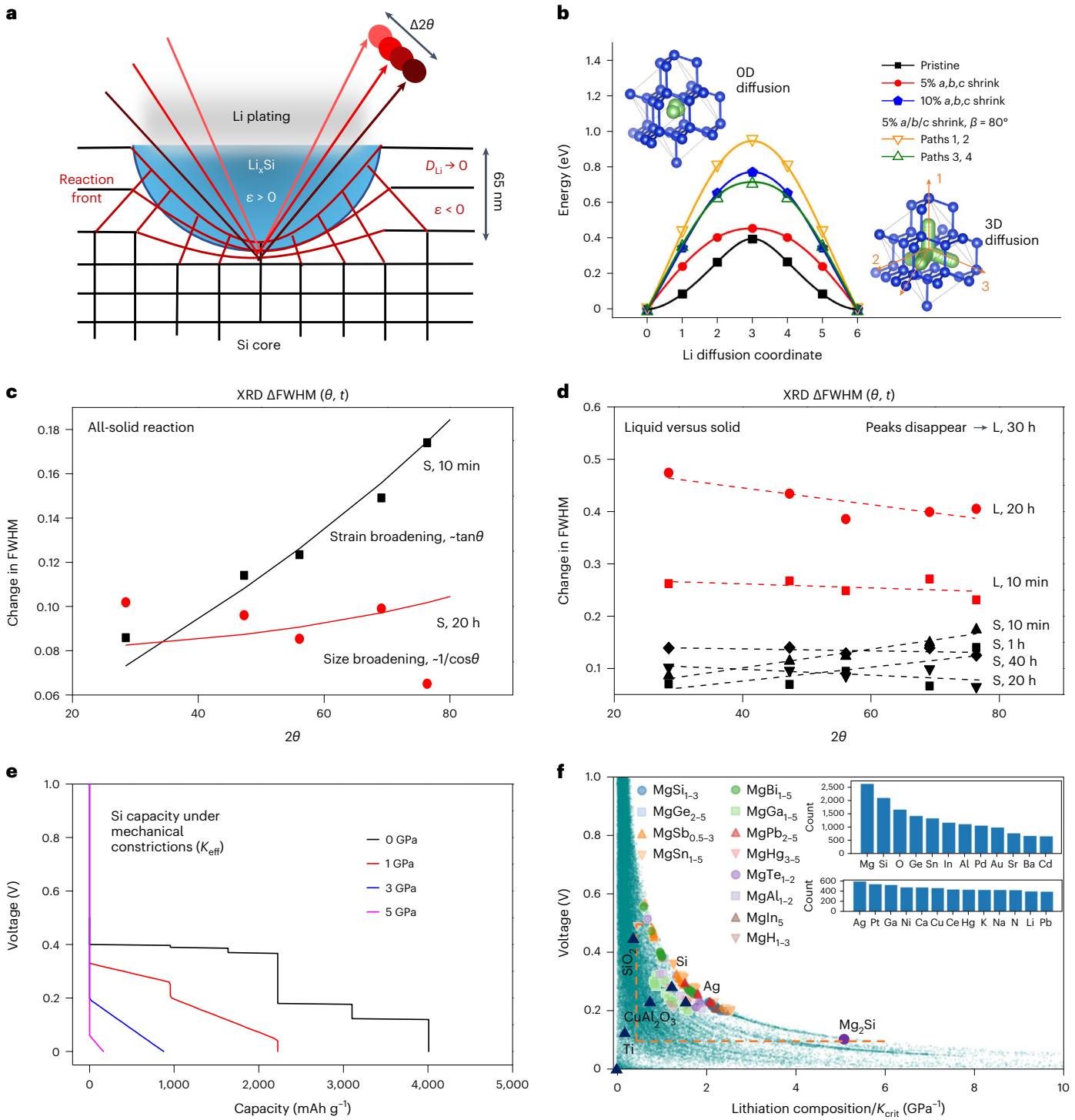

Fig. 3 | Constriction susceptibility of anode materials and diffusion-limiting process for Li plating. a, Illustration of lithiation reaction strain-induced, diffusion-limiting process. At the reaction front (red region), compressive strain causes Li diffusivity (D_{Li}) to approach zero, thus kinetically promoting Li plating at such surface nanosites. The effect also causes strain broadening ($\Delta 2\theta$) for Si XRD peaks. **b**, Diffusion pathway of Li in Si unit cell; 5–10% decrease in lattice parameters (a,b,c) isotopically led to an increase of 50–550 meV in the Li diffusion barrier. Additional shear ($\alpha = \beta = 90°$, $\gamma = 80°$) at 5% compressive strain still resulted in a large increase in the Li diffusion barrier. These cases reduce 3D to zero-dimensional (0D) diffusion pathways. **c**, Broadening of FWHM versus 2θ angle for Li–Si pressed together in the dry state after 10 min and 20 h, labelled as S-time, where S represents the all-solid state. The points are fitted using tanθ (strain broadening) and 1/cosθ (size broadening) along the solid lines. **d**, Broadening of FWHM versus 2θ angle for Li–Si pressed together in the dry state after 10 min, 1 h, 20 h and 40 h (labelled as S-times). In comparison, such pressed Li–Si layers were added by liquid electrolyte and then rested for 10 min, 20 h and 30 h (labelled as L-times). Dashed lines are for visual guidance only. **e**, Simulated voltage-capacity dependence of Si anode at different levels of mechanical constriction, where K_{eff} is the effective constriction module, ranging 0–5 GPa. **f**, High-throughput calculation results for voltage (y axis) and lithiation composition over K_{crit} (x axis) for anodic reaction versus Li metal anode for 59,524 material entries within the plotted axes range. Voltage is average lithiation voltage of a material versus Li$^+$/Li, and K_{crit} is the critical modulus at which lithiation reaction between Li metal and the material can be suppressed by mechanical constriction. Inset shows the elemental distribution of 11,568 material entries in the region between the dashed lines and the boundary of the highest lithiation energy per Li per unit constriction.

https://doi.org/10.1038/s41563-023-01722-x

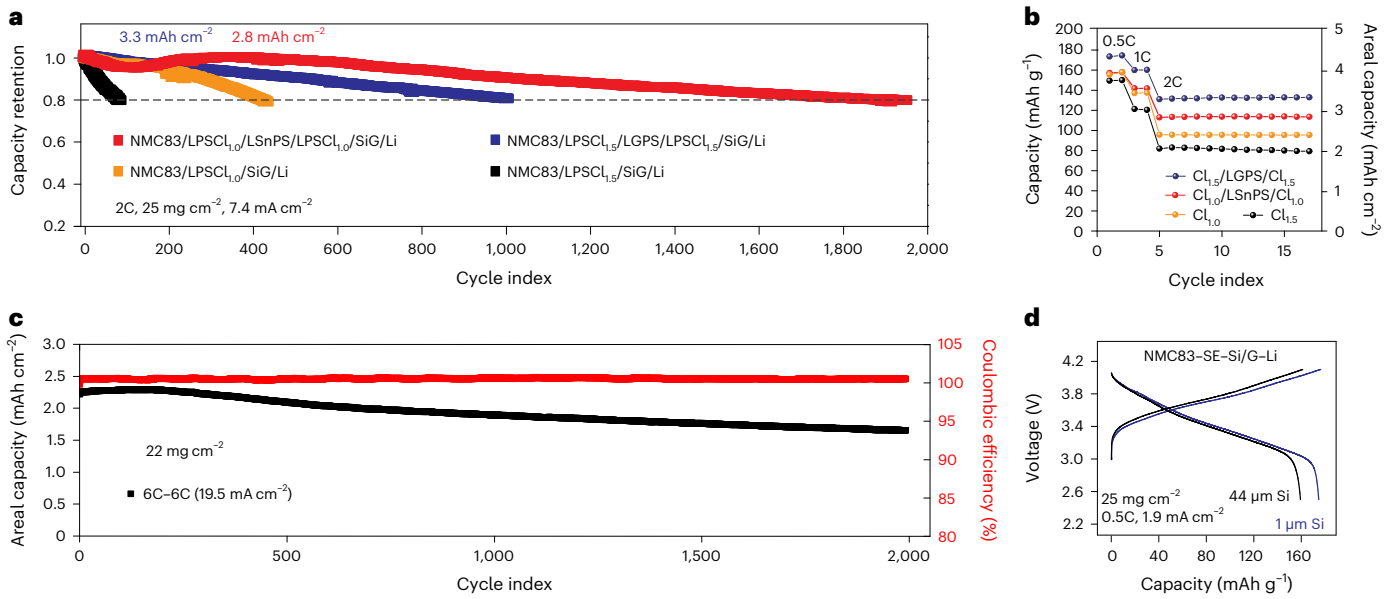

Fig. 4 | Coin cell cycling data utilizing constriction-susceptible anode design. **a**, Capacity retention comparison between single- and multi-SE-layer batteries with a SiG/Li anode, all at 25 mg cm^{-2} cathode loading, 7.4 mA cm^{-2} current density or 2C-rate and the same total thickness of electrolyte layer(s). The areal capacity of the 2,000-cycle battery is between 2.8 and 2.2 mAh cm^{-2}. Electrolyte chemical formulae: $Li_{5.5}PS_{4.5}Cl_{1.5}$ ($LSPCl_{1.5}$ or $Cl_{1.5}$), $Li_6PS_5Cl_{1.0}$ ($LPSCl_{1.0}$ or $Cl_{1.0}$). **b**, Specific capacity of four batteries at different C-rates showing that multilayer electrolytes offer higher capacity than a single layer, all at 25 mg cm^{-2} cathode loading. **c**, Capacity retention and Coulombic efficiency of a battery running at 6C–6C at 19.5 mA cm^{-2} with the structure Li/SiG-$Cl_{1.0}$–LGPS-$Cl_{1.0}$–NMC83 at 22 mg cm^{-2} cathode loading. **d**, Charge and discharge curves of multilayer batteries with Si of varying particle size between 1 and 44 μm. All batteries were tested at 55 °C.

design that combines the SiG-based Li metal anode of updated multi-layer electrolyte configuration[17] with new combinations of electrolyte layers, we obtained an impressive cycling performance at cathode loadings ≥15 mg cm^{-2}. Note that, here, graphite is mainly used to (1) prevent Li penetration through the Li foil during initial assembly under formation pressure[18] and (2) provide a better electron conduction pathway[7]. We also found reduced pore size in the SiG layer in the assembled battery in comparison with the pure Si layer, which would beneficially limit the Li-plating region closer to the surface lithiation sites of Si because Li plating occurs at the void region between Si particles rather than at the graphite region in the SiG layer (Figs. 1b,c and 2e and Extended Data Figs. 3 and 4).

Figure 4a shows the cycling performance of our solid-state batteries with a configuration of Li–SiG–SEs–NMC83 at a cathode loading of 25 mg cm^{-2}, with 80% capacity retention following either 1,000 or 2,000 cycles at a high current density of 7.4 mA cm^{-2} or 2 C-rate (the charge or discharge current divided by the battery's capacity to store an electrical charge). As expected, single-electrolyte layer configurations at the same total thickness of electrolyte layer showed markedly inferior cycling of <500 cycles at the same cathode loading and rate. Figure 4b further shows that multilayer design can deliver much higher capacity than the single-layer design at 1–2 C-rate, giving an areal capacity around 2–3 mAh cm^{-2} with good cycling performance (Fig. 4a,b). The difference in the performance of the multi-electrolyte layer here can be attributed to variation in the dynamic voltage and electrochemical stabilities that have been quantified previously both experimentally[10,17,19] and computationally[10]. The fact that our previous multi-electrolyte-layer strategy that was developed to prevent Li dendrite penetration of the Li metal anode still worked here also suggests that significant Li plating and stripping occurs in the current SiG anode running at higher current densities. At 6C charge and discharge the battery showed a capacity of >110 mAh g^{-1}, with 80% capacity retention obtained after 1,500 cycles (Fig. 4c) at a cathode loading of 22 mg cm^{-2} of NMC83 and high areal capacity of around 1.0–2.3 mAh cm^{-2}. Note that, when the SiG layer was replaced by a Si layer, cycling number was reduced to around 1,000 in our test. We also found that Si particle size (1–44 μm) has limited influence on the capacity of the full battery (Fig. 4d). Extended Data Fig. 7 provides further data on battery cycling, specifically in relation to high-loading (up to 7 mAh cm^{-2}), low-temperature (down to 0 °C) and fast-charging (up to 10 C-rate) capability.

A solid-state pouch cell was then made using NMC83 and Li metal with SiG anode protection. Cathode size in the pouch cell was 28 × 35 mm^2. Figure 5a shows the cycling performance of the pouch cell at an operational pressure of 25 MPa. The solid-state pouch cell was cycling at a high rate of 5C charge and 5C discharge, with the initial capacity around 125 mAh g^{-1} and capacity retention of around 92% after 2,000 cycles, 88% after 3,000 cycles and 80% after 6,000 cycles. The electrolyte-separator layers were made using a layer-by-layer slurry-casting method consisting of Li_6PS_5Cl, $Li_{10}SnP_2S_{12}$ and Li_6PS_5Cl with total separator thickness of around 75 μm (Fig. 5b,c). The energy density of the pouch cell was 218 Wh kg^{-1} without considering the pressure jig in the calculation (Extended Data Table 1) which, in principle, can be further improved by reducing separator thickness and operational pressure and increasing cathode loading.

Practical design strategies and use of materials other than Si

Rapid charging in alkaline metal-based batteries is dependent on two preconditions—rapid electrochemical kinetics and the prevention of Li dendrites. The Li–Si alloying reaction is relatively slower than Li plating and stripping[20–23], which is usually accompanied by pulverization of Si if it proceeds deeply, making it difficult to achieve rapid and stable cycling. Here we show that significant Li metal plating can be achieved through dynamic interaction with the shallow lithiation sites of partially prelithiated Si, yielding rapid cycling capability at high current density. This is a new capability and a mechanism beyond the Li–Si alloying reaction mentioned in either liquid-electrolyte[24] or solid-state

https://doi.org/10.1038/s41563-023-01722-x

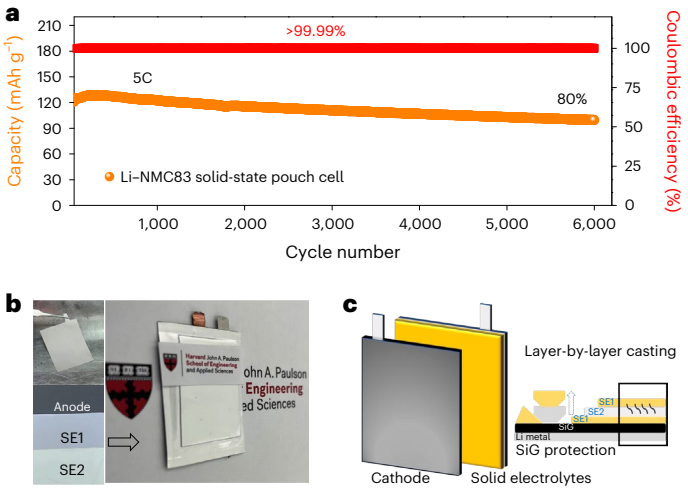

Fig. 5 | Pouch cell cycling data utilizing constriction-susceptible anode design. a, Cycling performance of solid-state pouch cell at 5C charge and discharge rates and an NMC83 cathode loading of 15 mg cm^{-2} at 55 °C and operational pressure 25 MPa. **b**, Photographs of a slurry-cast SiG anode covered by further casting of multi-electrolyte layers (top left), the edge of the anode multilayer configuration, solid-electrolyte type 1 (SE1) and type 2 (SE2) cast on top of each other (bottom left) and a solid-state pouch cell (right). **c**, Schematic illustration of pouch cell and layer-by-layer casting.

batteries[25]. Meanwhile, our design utilizes Li–Si alloying sites on a shallow surface of the Si particle to distribute current density, making it different from the conventional inert 3D scaffold that merely stores Li metal inside. The design not only circumvents Si swelling but also provides an ultrafast reaction pathway for rapid and stable cycling of Li metal in a solid-state battery.

Furthermore, because constriction susceptibility is applied through the effective modulus of the materials rather than by external pressure, there is still room for further reduction in operational stack pressure in principle. We demonstrate a 25 MPa operational pressure in Fig. 5 from our pouch cell test, a level that is already lower than that in coin cell tests that have an operational pressure of 50 MPa or above, both in the current work and in our previous reports[10,17]. Such a preferred Li plating was also found in the SiG anode working at 5 MPa (Extended Data Fig. 8), where the cycling stability in a solid-state pouch cell is reduced to 2,800 cycles at 5C charge and discharge. Compared with our solid-state coin cells using only dry ceramic powder to pave the electrolyte and electrode layers, a slurry-casting-based pouch cell method can provide denser layers through a polymer–ceramic composite, making it a promising candidate in the development of lower operational pressure. Future directions could also include the discovery of more deformative solid-electrolyte materials with optimized local viscoelasticity for constriction susceptibility, stronger polymer binders, dynamically stable cathode-coating materials[26] and polymer binders that can better accommodate the breathing dynamics of battery devices.

Going beyond micrometre-sized-Si, anode materials might also include a design strategy featuring coating of a constriction-susceptible anode material, such as Ag, to an insulating particle, such as SiO_2 or Al_2O_3 (Extended Data Fig. 9). Furthermore, although Ag is located near Si in Fig. 3f, these Ag nanoparticles may lithiate deeply as in the case of liquid electrolytes[23] because the initial lithiation sites may have already consumed the entire nanoparticle. Thus nano-Ag may undergo a lower K_{eff} and reduced kinetic dynamics between lithiation and plating than micrometre-sized Si. This different mechanism may be the reason for limitation in the rate of cycling performance previously found for Ag (60 nm) at the carbon anode at <1 C-rate under high cathode loading[27]. Larger Ag particles may show observable constriction susceptibility in regard to preferential Li plating in the initial electrochemical charge, especially at relatively high C-rates, and then further lithiate chemically with the plated Li. Micrometre-sized Ag, however, may be too ductile to provide a sufficient number of pores at the anode with the conventional procedure of rolling formation used in the battery industry. It is worth noting many Mg alloys are located near Si in Fig. 3f, suggesting them as promising anode materials with well-balanced voltage and constriction susceptibility. Our results here pave the way for the future design of solid-state batteries with superior rate performance at high loadings, where constriction of Si and other, more appropriate, materials for Li metal anode application could occur following the introduction of an advanced design of Li–anode interaction dynamics between lithiation and plating at both the material and device level.

Online content

Any methods, additional references, Nature Portfolio reporting summaries, source data, extended data, supplementary information, acknowledgements, peer review information; details of author contributions and competing interests; and statements of data and code availability are available at https://doi.org/10.1038/s41563-023-01722-x.

References

1. Pietsch, P. et al. Quantifying microstructural dynamics and electrochemical activity of graphite and silicon-graphite lithium ion battery anodes. *Nat. Commun.* **7**, 12909 (2016).
2. Goodenough, J. B. & Park, K. S. The Li-ion rechargeable battery: a perspective. *J. Am. Chem. Soc.* **135**, 1167–1176 (2013).
3. Li, S. et al. Developing high-performance lithium metal anode in liquid electrolytes: challenges and progress. *Adv. Mater.* **30**, 1706375 (2018).
4. Li, X. et al. Mesoporous silicon sponge as an anti-pulverization structure for high-performance lithium-ion battery anodes. *Nat. Commun.* **5**, 4105 (2014).
5. Wu, H. & Cui, Y. Designing nanostructured Si anodes for high energy lithium ion batteries. *Nano Today* **7**, 414–429 (2012).
6. Kim, J. S. et al. Three-dimensional silicon/carbon core-shell electrode as an anode material for lithium-ion batteries. *J. Power Sources* **279**, 13–20 (2015).
7. Xing, X. et al. Graphite-based lithium-free 3D hybrid anodes for high energy density all-solid-state batteries. *ACS Energy Lett.* **6**, 1831–1838 (2021).
8. Kim, H., Seo, M., Park, M. H. & Cho, J. A critical size of silicon nano-anodes for lithium rechargeable batteries. *Angew. Chem. Int. Ed. Engl.* **49**, 2146–2149 (2010).
9. Ye, L. et al. Toward higher voltage solid-state batteries by metastability and kinetic stability design. *Adv. Energy Mater.* **10**, 2001569 (2020).
10. Wang, Y., Ye, L., Chen, X. & Li, X. A two-parameter space to tune solid electrolytes for lithium dendrite constriction. *J. Am. Chem. Soc.* **2**, 886–897 (2022).
11. Fitzhugh, W., Ye, L. & Li, X. The effects of mechanical constriction on the operation of sulfide based solid-state batteries. *J. Mater. Chem. A* **7**, 23604–23627 (2019).
12. Fitzhugh, W., Chen, X., Wang, Y., Ye, L. & Li, X. Solid-electrolyte-interphase design in constrained ensemble for solid-state batteries. *Energy Environ. Sci.* **14**, 4574–4583 (2021).
13. Chen, X. et al. Reversible flat to rippling phase transition in Fe containing layered battery electrode materials. *Adv. Funct. Mater.* **28**, 1803896 (2018).
14. Chen, X. et al. Super charge separation and high voltage phase in Na_xMnO_2. *Adv. Funct. Mater.* **28**, 1805105 (2018).
15. Chen, Y. et al. Li metal deposition and stripping in a solid-state battery via Coble creep. *Nature* **578**, 251–255 (2020).

16. Masias, A., Felten, N., Garcia-Mendez, R., Wolfenstine, J. & Sakamoto, J. Elastic, plastic, and creep mechanical properties of lithium metal. *J. Mater. Sci.* **54**, 2585–2600 (2019).
17. Ye, L. & Li, X. A dynamic stability design strategy for lithium metal solid state batteries. *Nature* **593**, 218–222 (2021).
18. Su, Y. et al. A more stable lithium anode by mechanical constriction for solid state batteries. *Energy Environ. Sci.* **13**, 908–916 (2020).
19. Gil-González, E. et al. Synergistic effects of chlorine substitution in sulfide electrolyte solid state batteries. *Energy Storage Mater.* **45**, 484–493 (2022).
20. Yoshimura, K., Suzuki, J., Sekine, K. & Takamura, T. Measurement of the diffusion rate of Li in silicon by the use of bipolar cells. *J. Power Sources* **174**, 653–657 (2007).
21. Wang, M., Xiao, X. & Huang, X. Study of lithium diffusivity in amorphous silicon via finite element analysis. *J. Power Sources* **307**, 77–85 (2016).
22. Ding, N. et al. Determination of the diffusion coefficient of lithium ions in nano-Si. *Solid State Ionics* **180**, 222–225 (2009).
23. Yan, K. et al. Selective deposition and stable encapsulation of lithium through heterogeneous seeded growth. *Nat. Energy* **1**, 16010 (2016).
24. Ma, D., Cao, Z. & Hu, A. Si-based anode materials for li-ion batteries: a mini review. *Nanomicro Lett.* **6**, 347–358 (2014).
25. Tan, D. H. S. et al. Carbon-free high-loading silicon anodes enabled by sulfide solid electrolytes. *Science* **373**, 1494–1499 (2021).
26. Wang, Y., Ye, L., Fitzhugh, W., Chen, X. & Li, X. Interface coating design for dynamic voltage stability of solid state batteries. *Adv. Energy Mater*. https://doi.org/10.1002/aenm.202302288 (2023).
27. Lee, Y. G. et al. High-energy long-cycling all-solid-state lithium metal batteries enabled by silver–carbon composite anodes. *Nat. Energy* **5**, 299–308 (2020).

Methods

Synthesis

$Li_{5.5}PS_{4.5}Cl_{1.5}$ (LPSCl) was prepared by high-energy ball milling and a subsequent annealing process. Stoichiometric amounts of Li_2S (99.9% purity, Alfa Aesar), P_2S_5 (99% purity, Sigma-Aldrich) and LiCl (99% purity, Alfa Aesar) were milled for 16 h in a planetary PM200 (Retsch) under a protective Ar atmosphere, followed by sintering at 550 °C in a quartz tube.

Coin cell

A 0.63-cm-diameter Li foil (thickness 25 µm) was covered by a 0.79-cm-diameter SiG composite film with weight ratio 47.6:47.6:4.8% Si (1 µm; Skyspring Nanomaterials, Inc.), graphite (BTR) and polytetrafluoroethylene (PTFE). A Mg_2Si (Sigma-Aldrich) protection layer was mixed with graphite and PTFE at the same weight ratio. SiO_2 and Ag-coated SiO_2 (2 µm particle size, Cospheric LLC) were mixed with graphite and PTFE at a weight ratio of 19.0:76.2:4.8%. The cathode layer was made by mixing 30 wt% SE, 70 wt% single-crystal $LiNbO_3$-coated[28] $LiNi_{0.83}Mn_{0.1}Co_{0.07}O_2$ (1–5 µm particle size, MSE Supplies) and an additional 3 wt% PTFE with an active material loading of 10–60 mg cm^{-2}. For the single-layer design, 120 mg of either LPSCl1.0 or LPSCl1.5 was used as the electrolyte; for the multilayer design, 20 mg of LPSCl1.5 and 100 mg of either $Li_{10}GeP_2S_{12}$ (LGPS) or $Li_{10}SnP_2S_{12}$ (LSnPS) were used. The full battery, with structure Li–SiG–LPSCl1.5–LGPS–LPSCl1.5–NMC83, was pressed together in a home-made pressurized cell at 400 MPa and maintained at 50 MPa during testing. Nominal negative to positive (NP) electrode capacity ratio was controlled at 0.3–1.5 and was calculated based on the practical capacities of Si (nearly 3,000 mAh g^{-1}) and NMC83 (200 mAh g^{-1}). All batteries were assembled in an Ar-atmosphere glovebox with the humidity of the battery-testing environment controlled inside a Memmert hpp110. Battery testing was conducted using an Arbin instrument at either 0, 35 or 55 °C. Cut-off voltage was set between 2.5 and 4.1 V for normal-rate cycling and between 2.0 and 4.35 V for high-rate cycling. Liquid cells were created using either Li (Fig. 1d) or SiG (Extended Data Fig. 2a–c) as the anode and 1 M $LiPF_6$ in ethylene carbonate and dimethyl carbonate (EC/DMC, v/v =1:1) as the electrolyte.

Asymmetric battery

Asymmetric coin cell battery (for example, Fig. 1) refers to a configuration of Li/G–SEs–(anode protection layer). Li/G with a capacity of 2.5:1 was used as the anode, and 20 mg of LPSCl1.5 and 100 mg of LGPS as electrolytes. Different anode protection materials (for example, Si and Mg_2Si) were mixed with graphite and PTFE at a ratio of 47.6:47.6:4.8%. These layers were stacked and pressed into a pellet at 400 MPa and maintained at 50 MPa during testing. Asymmetric batteries were tested at 0.2 mA cm^{-2} at room temperature.

Pouch cell

An anode protection layer and three SE layers were cast sequentially onto Li foil. To prepare slurry for the anode protection layer, 50 wt% Si powder (1 µm), 50 wt% graphite powder and an additional 2.5 wt% acrylate-based polymer binder were mixed with anhydrous *p*-xylene and isobutyl isobutyrate (1:1 v/v) using a planetary centrifugal mixer, then Li_6PS_5Cl, $Li_{10}SnP_2S_{12}$ and Li_6PS_5Cl layers were cast on to the anode. Following four-layer coating the film was then transferred to a vacuum oven to dry thoroughly at 60 °C for 12 h. Dried multilayer film was cut, using a pneumatic punch machine, into a specific size of 35 × 28 mm^2 for pouch cell fabrication. The cathode comprised 70% NMC83, 30% LPSCl and 2.5% additional binder, and cathode active loading was 15 mg cm^{-2}. The anode/SE and cathode films were stacked and pressed at 350 MPa and 70 °C and then tested at either 25 MPa or 5 MPa operational pressure.

X-ray photoelectron spectroscopy. XPS was conducted using a Thermo Scientific K-Alpha$^+$ with spot size 400 µm. A vacuum transfer module was used to transfer samples from the glovebox to the XPS chamber. Samples were not exposed to air during either XPS sample transfer or measurement. Ar ion milling was applied, with energy 0.5 keV and current ~0.6 µA, for 500–1,000 s. Etch rate was estimated based on ~0.52 Å s^{-1} reported in the literature from the reference sample of SiO_2 (refs. 29,30).

X-ray diffraction. XRD was conducted on a Rigaku Miniflex with Cu-Kα. Measurements were taken within a 2θ range, from 10 to 80° at 40 kV and 15 mA. The sample was sealed with a Kapton film in the glovebox before transfer to the XRD. For the solid-state test shown in Fig. 3, Si was pressed together with Li at 400 MPa and held at 50 MPa, with Li:Si capacity of 2:1. For Si with liquid added, Si was pressed with Li at 400 MPa, held at no external pressure and a drop of liquid electrolyte added, with Li:Si capacity of 2:1. Broadening of FWHM was calculated based on a comparison with pristine Si following pressing at 400 MPa.

SEM–FIB–energy-dispersive X-radiography

A FEI Helios 660 was used for FIB–SEM imaging. The pristine material and cycled pellets were transferred from an Ar-filled glovebox using a sealed plastic bag. The sample was exposed to air for 1–2 min during transfer. Pt predeposition and Ga^+ milling procedures were conducted to create a cleaned cross-section region under different currents. SEM–energy-dispersive X-ray imaging was conducted using the inbuilt energy-dispersive X-ray analysis tools and detector of the instrument. The batteries for SEM–FIB imaging were tested at room temperature.

TEM

The lithiated anode was milled by FIB till it reached a thickness suitable for (S)TEM and EELS measurements; thickness, as confirmed by both SEM–FIB and STEM–EELS, was 65 nm. Using EELS, thickness is calculated based on a convergence angle of 30 mrad, collection angle 43 mrad and $\ln(I_t/I_0)$ = ~0.54, where I_t and I_0 are total spectrum integral and zero-loss integral, respectively[31]. Such a thickness can provide a sufficient signal for the detection of Li. (S)TEM, high-resolution TEM and EELS were conducted on an ARM 200 with voltage 200 kV.

Computational methods

The effective modulus multiplying local strain (ϵK_{eff}) can often be larger than the actual local stress (σ_{loc}) in solid-state batteries because ϵK_{eff} must also include the effective contribution from the kinetic stability effect $\epsilon K_\epsilon^{D\to 0}$, where $\epsilon K_{\text{eff}} = \sigma_{\text{loc}} + \epsilon K_\epsilon^{D\to 0}$ and $D \to 0$ denote that Li-ion diffusivity is approaching zero at the reaction front. For Si, σ_{loc} was measured at around 1.0 GPa (refs. 32,33). The term $\epsilon K_\epsilon^{D\to 0}$, which assumes importance in solid-state batteries, is thus not local stress although with a unit of GPa; rather, it is an effective contribution from the reaction strain-induced, diffusion-limiting process to the reaction front[9,26]. Our simulation estimates that the magnitude of $\epsilon K_\epsilon^{D\to 0}$ is comparable to local stress.

Voltage, capacity and K_{crit} were calculated as follows. Electrochemical reaction energy (G) and number of charge transfer (n) at 0 V versus Li^+/Li was first calculated by construction of a phase diagram using the Python Materials Genomics library[34]. Voltage (U) was then calculated using the Nernst equation as $G = -nFU$, where F is the Faraday constant. Lithiation composition was calculated according to the number of charge transfer. Because $K_{\text{crit}} = -G/(V \times \varepsilon)$, where ε is reaction strain and V the reference volume of materials, we have $U \times n/K_{\text{crit}} = \varepsilon \times V/F$, which is the product of the *x*- and *y*-axis values in Fig. 3f. For electrochemical reactions at 0 V the reaction equations are similar, which means that reaction volume change ($\varepsilon \times V$) is similar among many materials. $U \times n/K_{\text{crit}}$—that is, voltage × lithiation composition/K_{crit}—will thus be almost a constant for one family type of materials, giving the reciprocal relation shown in Fig. 3f. All density functional theory simulations were performed using the Vienna Ab initio Simulation Package implementing the pseudopotential plane wave method[35,36].

Perdew–Burke–Ernzerhof generalized-gradient approximation was used for exchange-correlation energy[37]. The nudged elastic band method was employed to calculate Li-ion diffusion barrier[38].

Data availability

The data that support the findings of this study are available from the corresponding author on reasonable request.

References

28. Xin, F. et al. Li-Nb-O coating/substitution enhances the electrochemical performance of the $LiNi_0.8Mn_0.1Co_0.1O_2$ (NMC 811) cathode. *ACS Appl. Mater. Interfaces* **11**, 34889–34894 (2019).
29. Chang, H. Y. et al. X-ray photoelectron spectroscopy equipped with gas cluster ion beams for evaluation of the sputtering behavior of various nanomaterials. *ACS Appl. Nano Mater.* **5**, 4260–4268 (2022).
30. Kyoung, Y. K. et al. Electronic structures of SiO_2 thin films via Ar gas cluster ion beam sputtering. *Surf. Interface Anal.* **46**, 58–61 (2014).
31. Ghosh, T., Bardhan, M., Bhattacharya, M. & Satpati, B. Study of inelastic mean free path of metal nanostructures using energy filtered transmission electron microscopy imaging. *J. Microsc.* **258**, 253–258 (2015).
32. Sethuraman, V. A., Chon, M. J., Shimshak, M., Srinivasan, V. & Guduru, P. R. In situ measurements of stress evolution in silicon thin films during electrochemical lithiation and delithiation. *J. Power Sources* **195**, 5062–5066 (2010).
33. Choi, Y. S., Pharr, M., Oh, K. H. & Vlassak, J. J. A simple technique for measuring the fracture energy of lithiated thin-film silicon electrodes at various lithium concentrations. *J. Power Sources* **294**, 159–166 (2015).
34. Ong, S. P. et al. Python Materials Genomics (pymatgen): a robust, open-source python library for materials analysis. *Comput. Mater. Sci.* **68**, 314–319 (2013).
35. Kresse, G. & Furthmüller, J. Efficiency of ab-initio total energy calculations for metals and semiconductors using a plane-wave basis set. *Comput. Mater. Sci.* **6**, 15–50 (1996).
36. Vargas-Hernández, R. A. Bayesian optimization for calibrating and selecting hybrid-density functional models. *J. Phys. Chem. A* **124**, 4053–4061 (2020).
37. Perdew, J. P., Burke, K. & Ernzerhof, M. Generalized gradient approximation made simple. *Phys. Rev. Lett.* **77**, 3865–3868 (1996).
38. Wan, W., Zhang, Q., Cui, Y. & Wang, E. First principles study of lithium insertion in bulk silicon. *J. Phys. Condens. Matter* **22**, 415501 (2010).

Acknowledgements

We thank J. Vlassak and F. Spaepen for helpful discussions. This work was supported by the Department of Energy Vehicle Technology Office, Harvard Climate Change Solutions Fund and Harvard Data Science Initiative Fund. SEM and TEM experiments were conducted at the Center for Nanoscale Systems at Harvard University, supported by the National Science Foundation. This work was also supported by computational resources from the Extreme Science and Engineering Discovery Environment Stampede and Frontera supercomputers.

Author contributions

X.L. conceived the project and supervised all aspects of the research. L.Y., Y.L. and J.L. performed experiments. Y.W. performed computations. J.L performed TEM. L.Y. and Y.L. made the coin cell and pouch cell. L.Y. and X.L. analysed results and wrote the paper, with contributions from all co-authors.

Competing interests

X.L., L.Y., Y.L. and Y.W. report a US provisional patent application: Fast cycling of lithium metal solid-state battery at high loading (filed 29 November 2022; application serial no. 63/428,634). The other authors declare no competing interests.

Additional information

Extended data is available for this paper at https://doi.org/10.1038/s41563-023-01722-x.

Correspondence and requests for materials should be addressed to Xin Li.

Peer review information *Nature Materials* thanks the anonymous reviewers for their contribution to the peer review of this work.

https://doi.org/10.1038/s41563-023-01722-x

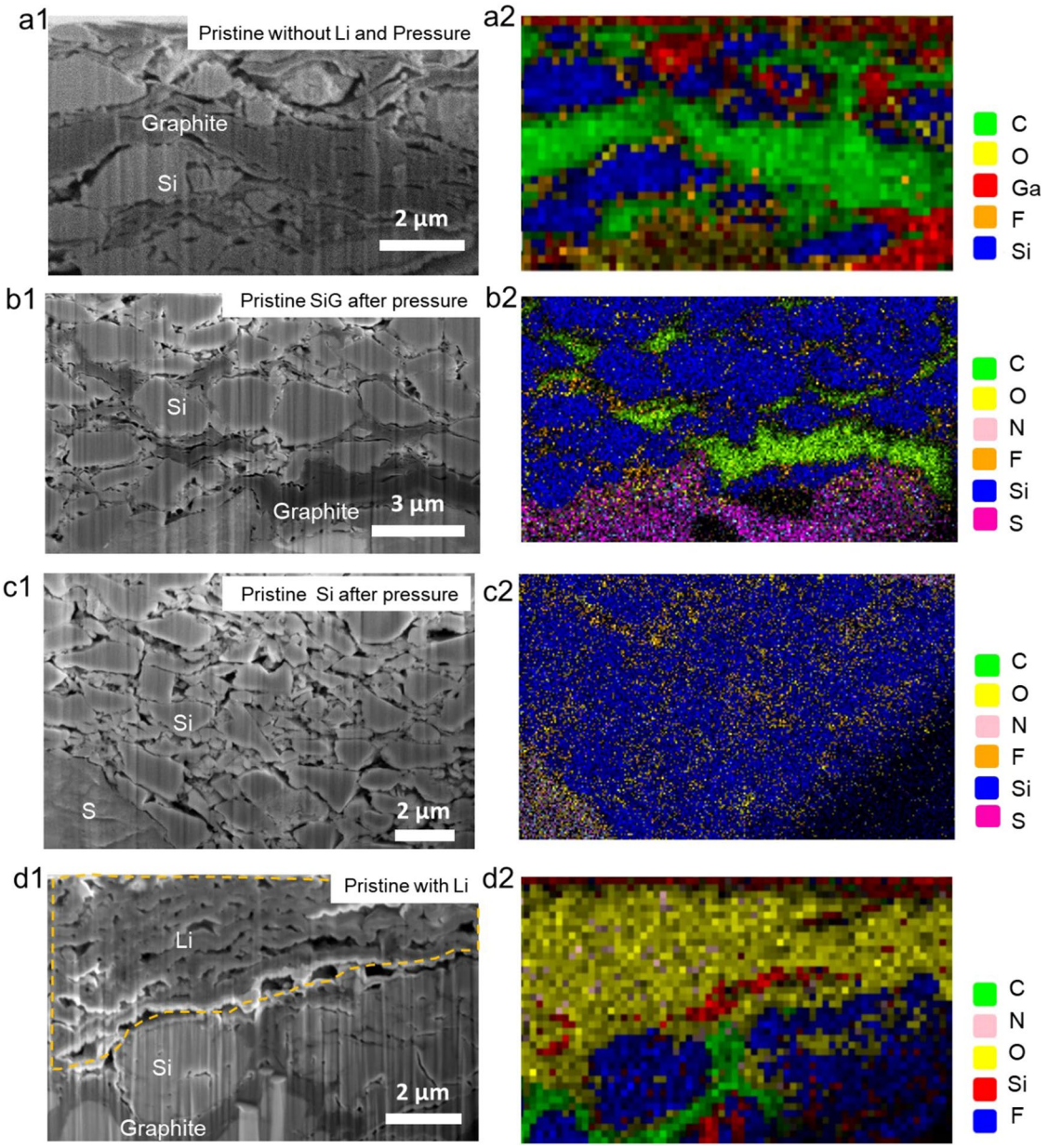

Extended Data Fig. 1 | The FIB-SEM and EDS mapping of Silicon/Graphite (SiG) layer with and without interfacing with Li metal foil. To further confirm that the oxygen EDS signal is mainly contributed by lithium metal, the cross-sections SEM and EDS analysis of pristine SiG composites with and without a lithium metal anode foil being directly added beneath the SiG layer are compared, where major oxygen and nitrogen signals are only observed from the added lithium metal foil. **(a)** SiG film without lithium metal foil and does not undergo formation pressure. **(b)** SiG film **(c)** Si film without lithium metal foil and undergoes formation pressure. **(d)** SiG film with lithium metal foil and undergoes formation pressure. F is from PTFE binder and Ga is from FIB ion source.

https://doi.org/10.1038/s41563-023-01722-x

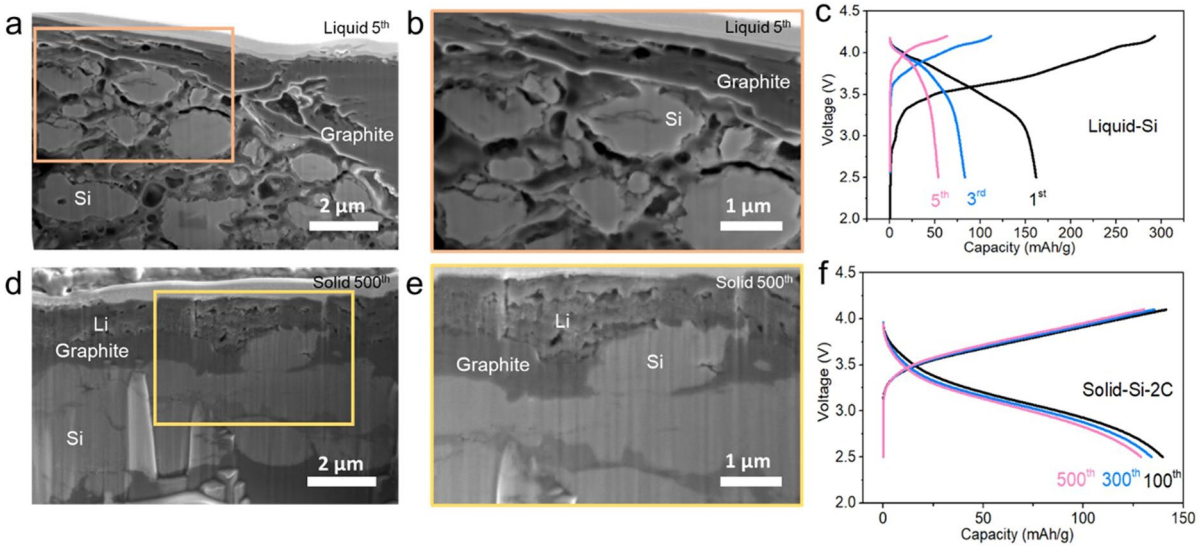

Extended Data Fig. 2 | SEM of cycled SiG in liquid- and solid-state batteries. When $LiNi_{0.83}Mn_{0.06}Co_{0.11}O2$ (NMC83) cathode is paired with SiG anode in a liquid electrolyte battery, pulverization of Si particles can be observed after just 5 cycles, accompanied by the poor cycling performance. In contrast, Si stays in an intact state in solid state batteries, with no cracks, pulverization, or irregular edges being found in the FIB-SEM images of Si particles after 500 cycles. **(a-b)** FIB-SEM image of SiG anode after the battery of SiG-liquid electrolyte-NMC83 (cathode loading = 25 mg/cm^2) running for 5 cycles. **(c)** Charge and discharge curve for the battery of SiG-EC/DMC/1 M $LiPF_6$-NMC83, where Si is micron-sized. **(d-e)** The FIB-SEM image of SiG anode after 500th cycling. The battery is with the structure of Li(25 um)/SiG-LPSCl-LGPS-LPSCl-NMC83 (cathode loading = 25 mg/cm^2) with a nominal NP ratio of 1.5. **(f)** Charge and discharge profile of the solid-state battery at 55 °C at 2 C, which is also the battery used for STEM-EELS in Fig. 2a. Note that the NP of 1.5 was hypothetically calculated based on the Si practical capacity of 3000 mAh/g and NMC83 capacity of 200 mAh/g.

https://doi.org/10.1038/s41563-023-01722-x

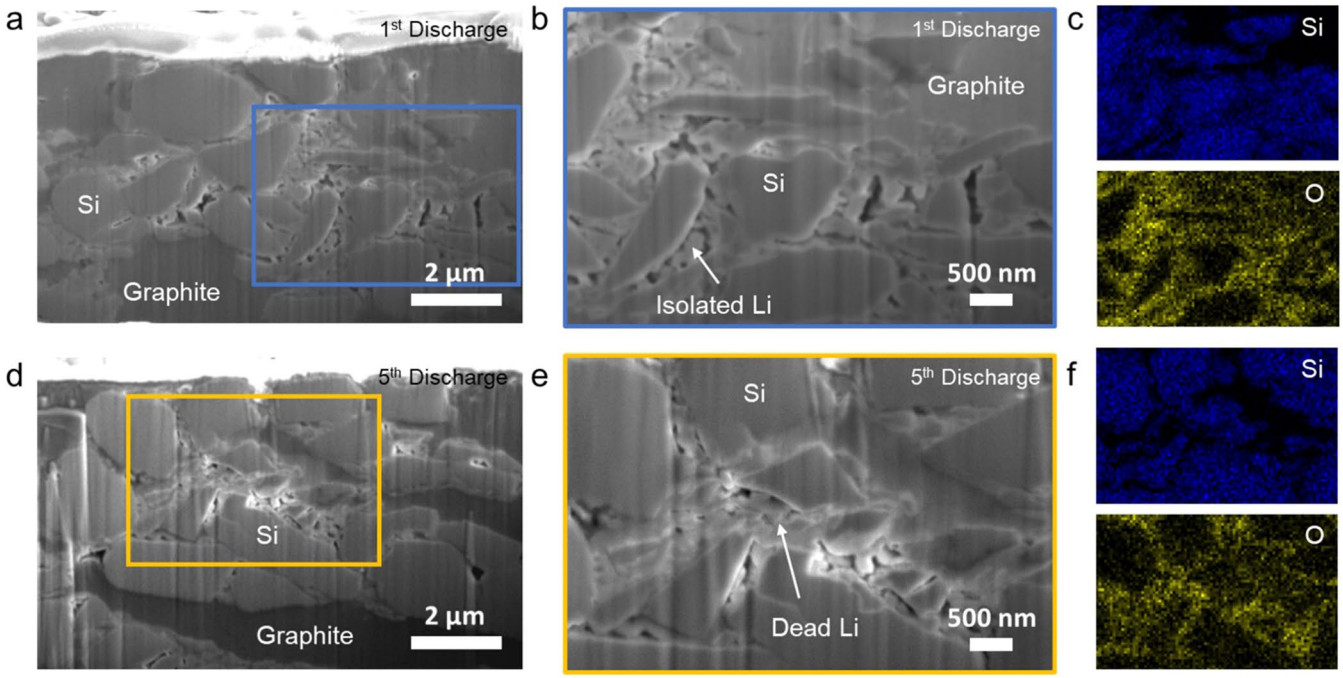

Extended Data Fig. 3 | Li plating between Si particles observed from SEM images of cycled SiG at different cycling stages in solid-state batteries. The FIB-SEM images and EDS mapping of SiG anode after the 1st **(a, b, c)** and the 5th **(d, e, f)** discharge. The batteries are with the structure of SiG-LPSCl-LGPS-LPSCl-NMC83 (loading = 25 mg/cm^2) with a nominal NP ratio of 1.5. The batteries were cycled at room temperature at 0.5 C.

https://doi.org/10.1038/s41563-023-01722-x

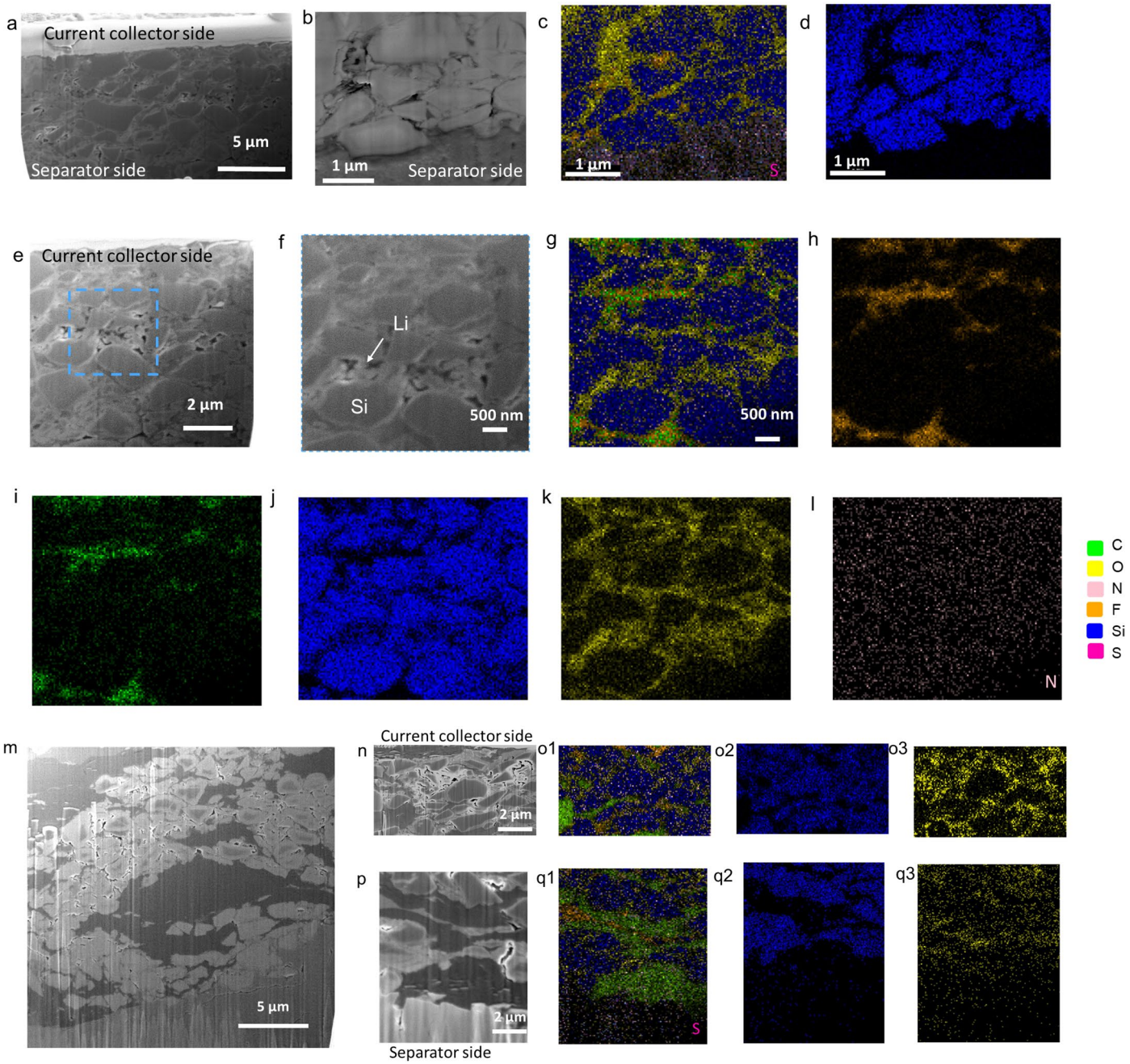

Extended Data Fig. 4 | Li plating between Si particles observed from SEM images and EDS mapping of Si and SiG at large scales. (a) FIB-SEM image of pure Si after charge from current collector side to separator side. **(b-d)** SEM and EDX on the separator side. **(e-l)** SEM and EDX on the current collector side. The battery is with the structure of Si-LPSCl-LGPS-LPSCl-NMC83 (loading = 25 mg/cm^2) with a nominal NP ratio of 1.5 and charged at 3.8 V at 0.5 C-rate at room temperature. **(m)** FIB-SEM image of pure **SiG** after charge from current collector side (top) to separator side (bottom). **(n-o)** SEM and EDX on the current collector side. **(p-q)** SEM and EDX on the separator side. The battery is with the structure of SiG-LPSCl-LGPS-LPSCl-NMC83 (loading = 25 mg/cm^2) with a nominal NP ratio of 1.5 and charged at 3.8 V at 0.5 C-rate at temperature.

https://doi.org/10.1038/s41563-023-01722-x

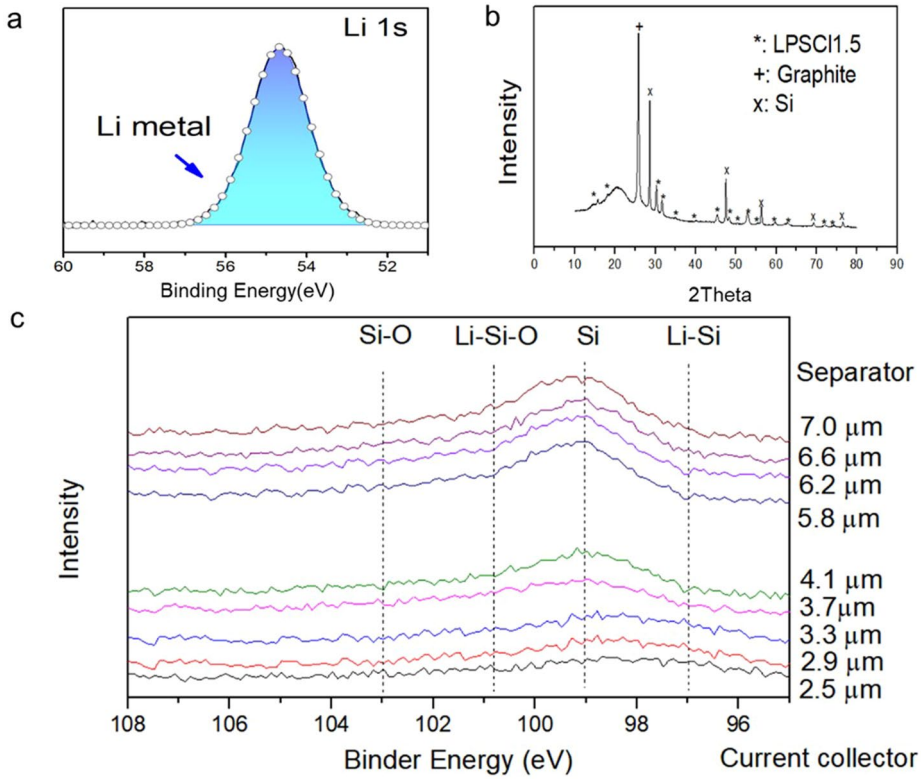

Extended Data Fig. 5 | Li plating and significant amount of unreacted Si observed from XPS, XRD, and XPS depth profile of SiG anode after lithiation process. (a) XPS measurement of Li 1 s signal from SiG in an NMC-SEs-SiG solid state battery with nominal NP ratio = 1.5 after the 1st charge at 0.5 C-rate at room temperature, showing the existence of Li metal. Since no Li layer was assembled on the anode side initially, this further confirms the plating of Li metal to the current collector side of the SiG layer from charging the cathode. **(b)** XRD of SiG from the above charged battery, clearly showing the Si phase rather than the lithiated alloying phase. **(c)** XPS depth profile of SiG anode after the 1st charge at higher milling energy for longer duration to investigate across the entire SiG electrode. The majority of Si peak throughout the SiG layer indicates that the lithiation of Si across the entire anode is significantly constricted. The sputtered thickness is estimated based on the 0.7 nm/s sputtering rate for Si, giving the number (μm) on the right side that is the thickness sputtered away from the current collector side. Note that the total thickness of the original SiG layer is ~10 μm. The battery is with the structure of SiG-LPSCl-LGPS-LPSCl-NMC83 (loading = 25 mg/cm^2) with a nominal NP ratio of 1 and charged at 4.1 V at 0.5 C-rate at room temperature.

https://doi.org/10.1038/s41563-023-01722-x

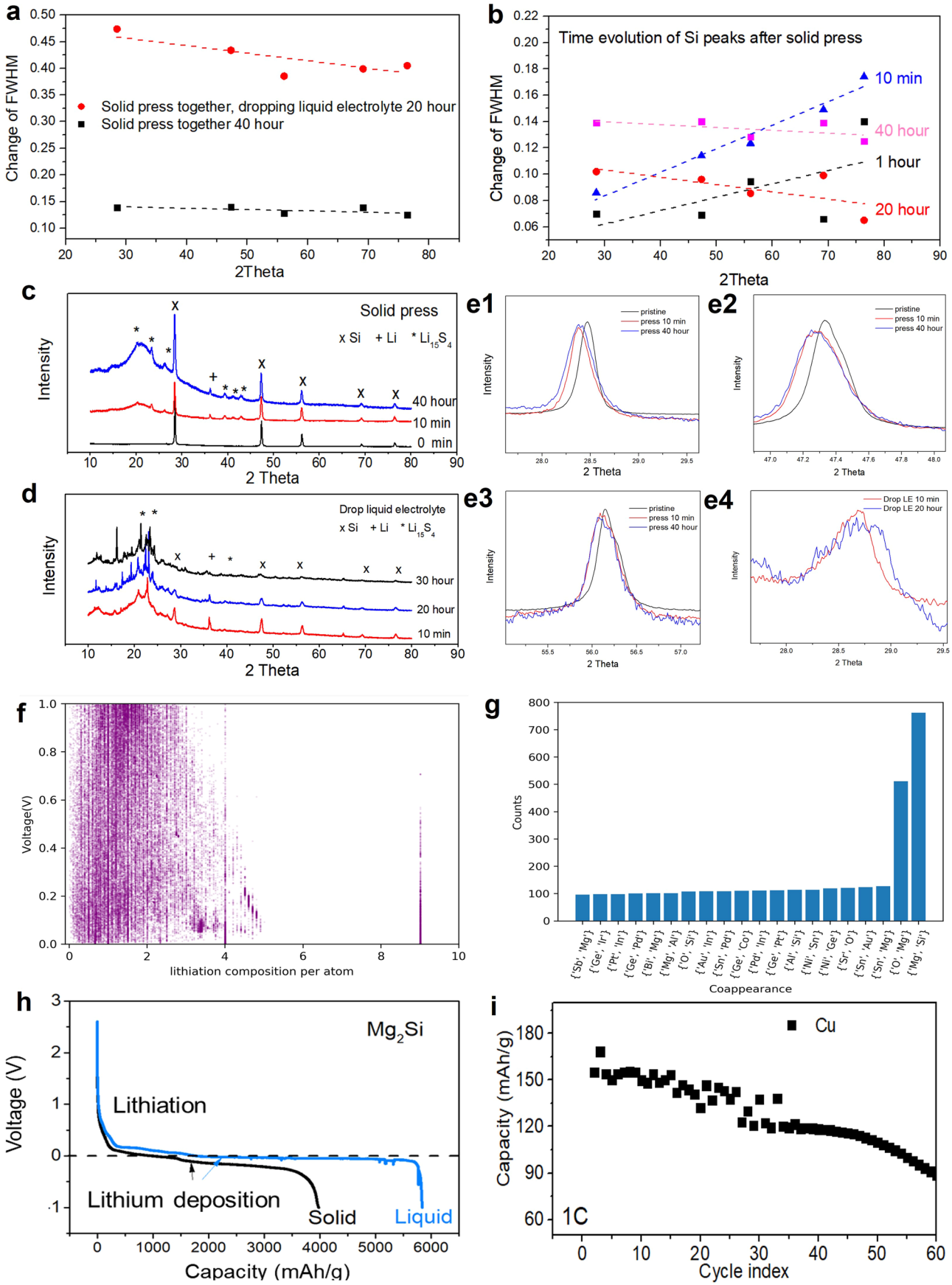

Extended Data Fig. 6 | See next page for caption.

https://doi.org/10.1038/s41563-023-01722-x

Extended Data Fig. 6 | Behaviors regarding constriction susceptibility for Si, Mg_2Si, and Cu in experiment, and computational prediction of such behaviors for more materials. (a) Change of XRD FWHM of Si powder in a solid layer pressed with Li metal solid layer at 400 MPa and held at 50 MPa for 40 hours (solid press), compared with that of such solid-pressed Si-Li interface after dropping liquid electrolyte (LE) and holding for 20 hours without external pressure. **(b)** Time evolution of XRD FWHM change for solid-pressed Si with Li metal after 10 min, 1 h, 20 h, and 40 h. **(c)** XRD peaks of Si after solid-pressing with Li metal and holding for 0 min, 10 min, and 40 hours. **(d)** XRD peaks of solid-pressed Si after dropping LE for 10 min, 20 min, and 30 hours. **(e1-e3)** Illustration of the time evolution of different XRD peaks in (c), which were used to plot ΔFWHM in (b). **(e4)** The time evolution of a XRD peak in (d) at 10 min and 20 h. The peak almost disappears after 30 hours. **(f)** Voltage v.s. lithiation composition per atom for materials with voltage between 0-1 V, and with capacity between 0-10000 mAh/g. **(g)** Two elements coappearance between the dashed lines in Fig. 3f. Only compounds with bandgap less than 1.5 eV are counted. **(h)** Electrochemical profiles for discharging Li toward Mg_2Si in liquid-state and solid-state battery systems at 0.2 mA cm^{-2} at room temperature. Mg_2Si is on the boundary but to the far right of Si in Fig. 3f. The lithiation capacity originally located above 0 V in the liquid electrolyte battery is largely suppressed in the solid-state battery, which is replaced by the lithium plating capacity below 0 V. This suggests that due to the much lower lithiation voltage and much higher constriction-susceptibility, Mg_2Si intrinsically prefers Li plating, or with a much less active alloying preference than Si. Thus, lithium plating from Mg_2Si will benefit less from the homogeneous current density distribution from the surface lithiation sites than Si. **(i)** Cyclig performance at 1 C-rate at 55 °C of battery with a structure of (Cu particle and graphite mixture)-SEs-NMC83 (cathode loading = 15 mg/cm^2).

https://doi.org/10.1038/s41563-023-01722-x

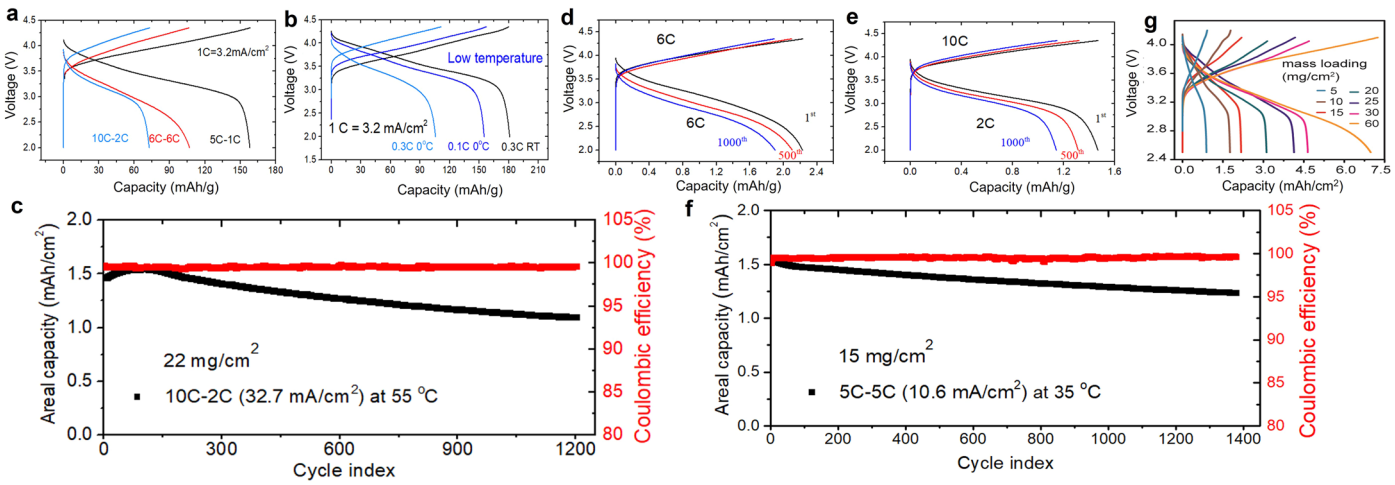

Extended Data Fig. 7 | Cycle performance of solid-state batteries toward high C-rate, high loading, and lower temperature. (a) Charge and discharge curves of solid state batteries at 5-10 C-rates and a NMC83 cathode loading of 22 mg/cm^2 at 55 °C, where 1 C = 3.2 mA/cm^2. The battery can deliver over 157 mAh/g at 5 C charge and 1 C normal discharge. **(b)** Low temperature voltage profiles of solid-state batteries with Li/SiG as anode and cathode loading of 22 mg/cm^2. The discharge capacity of the battery at 0 °C is 154 mAh/g. **(c)** Capacity retention and coulombic efficiency of battery running at 10 C (charge) -2C (discharge) at 55 °C. At 10 C charge and 2 C discharge a 75% retention after 1200 cycles was obtained. **(d-e)** Charge and discharge curves for Li/SiG-SEs-NMC83 (22 mg/cm^2 loading) battery running at 6C-6C (corresponding to Fig. 4c) and 10C-2C (corresponding to Extended Data Fig. 7c). It is worth emphasizing that the current densities for 6 C and 10 C here are extremely high at 19.5 and 32.7 mA/cm^2, respectively. **(f)** Capacity and coulombic efficiency of battery (NMC83 cathode loading = 15 mg/cm^2) running at 5C-5C at a lowered temperature of 35 °C (80% after 1400 cycles). **(g)** Charge and discharge curves of multilayer batteries with different cathode mass loading up to 60 mg/cm^2 and areal capacity up to 7 mAh/cm^2 at 0.5 C. The nominal NP ratio is kept at 1.5 for all batteries.

https://doi.org/10.1038/s41563-023-01722-x

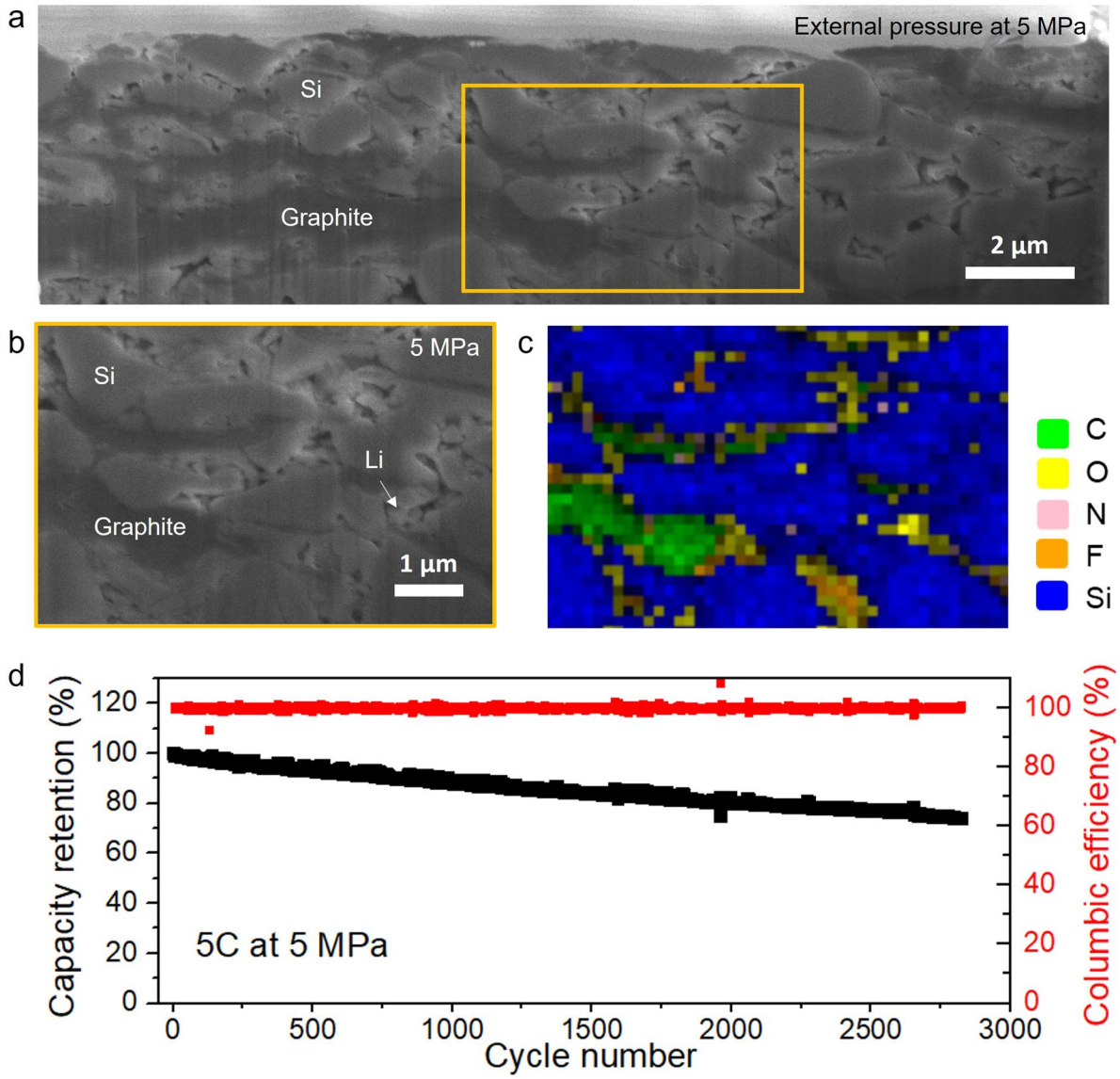

Extended Data Fig. 8 | Morphology and chemistry of SiG anode after discharging at low operational pressure. The FIB-SEM **(a,b)** and EDS mapping **(c)** of SiG anode after discharging at 5 MPa. The battery is with the structure of SiG-LPSCl-LGPS-LPSCl-NMC83 (loading = 25 mg/cm^2) with a nominal NP ratio of 1.5 and was cycled at room temperature at 0.5 C. (**d**) Pouch cell with the structure of Li-SiG-SEs-NMC83 (loading = 15 mg/cm^2) cycled at 5C charge and discharged at 5 MPa and 55 °C, with initial areal capacity = 1.36 mAh/cm^2.

https://doi.org/10.1038/s41563-023-01722-x

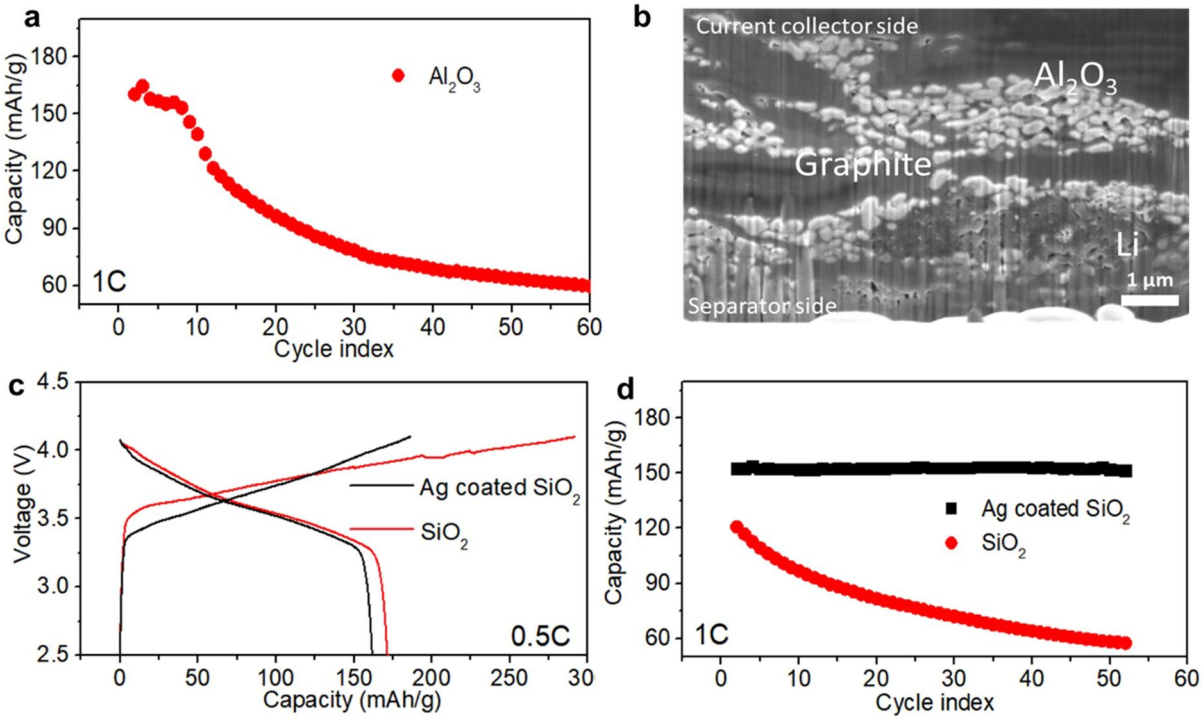

Extended Data Fig. 9 | Cycle performance of batteries with SiO_2, Al_2O_3, and Ag coated SiO_2 at anode, and the morphology analysis. (a) Cyclig performance at 1 C of a solid-state battery with Al_2O_3 particles at anode. The battery structure is Al_2O_3&Graphite mixture-SEs-NMC83 (loading = 15 mg/cm^2). A short circuit was observed after a few cycles, as lithium plates at the unwanted interface to the electrolyte layer due to a lack of ionic and electronic conductivity in Al_2O_3. Note that this is different from the diffusion limit to further lithiation discussed for Si, where both Li diffusion and electron conduction can still happen at the surface of Si particles. **(b)** FIB-SEM image of the Al_2O_3 layer after the 1st charge of a solid-state battery. **(c)** The first charge and discharge profiles at 0.5 C and **(d)** cylicng performance at 1 C of solid-state batteries with Ag coated SiO_2 at anode, in comparision that with bare SiO_2. The battery structure is SiO_2&Graphite mixture-SEs-NMC83 (loading = 15 mg/cm^2). A short circuit was observed at the initial charge for uncoated SiO_2, similar to bare Al_2O_3. In contrast, coating Ag to SiO_2 particles can make the battery run without a short circuit, but the migration of the coating layer with cycling could be an engineering challenge to solve in the future.

https://doi.org/10.1038/s41563-023-01722-x

Extended Data Table 1 | Energy density of the solid-state pouch cell

Cathode	Active Material Loading	15 mg/cm^2
	Active Material wt%	68.2%
	Thickness	70-85 µm
Separator	Thickness	75 µm
Anode	Active Material Loading	1.5 mg/cm^2
	Active Material wt%	48.75%
	Thickness	20-35 µm
Current collector	Al Thickness	12 µm
	Cu Thickness	10 µm
Total Energy		10.8 mWh/cm^2
Total Weight		49.5 mg/cm^2
Energy density		218 Wh/kg